JACS
JOURNAL OF THE AMERICAN CHEMICAL SOCIETY
Article
pubs.acs.org/JACS

Thermal Conversion of Core–Shell Metal–Organic Frameworks: A New Method for Selectively Functionalized Nanoporous Hybrid Carbon

Jing Tang,[†,‡] Rahul R. Salunkhe,[†] Jian Liu,[§] Nagy L. Torad,[∥] Masataka Imura,[†] Shuhei Furukawa,[⊥] and Yusuke Yamauchi*[,†,‡]

[†]World Premier International (WPI) Research Center for Materials Nanoarchitectonics (MANA), National Institute for Materials Science (NIMS), 1-1 Namiki, Tsukuba, Ibaraki 305-0044, Japan

[‡]Faculty of Science and Engineering, Waseda University, 3-4-1 Okubo, Shinjuku, Tokyo 169-8555, Japan

[§]Department of Chemical Engineering, Curtin University, Perth, Western Australia 6845, Australia

[∥]Chemistry Department, Faculty of Science, Tanta University, Tanta 31527, Egypt

[⊥]Institute for Integrated Cell-Material Sciences (WPI-iCeMS), Kyoto University, Yoshida, Sakyo, Kyoto 606-8501, Japan

Supporting Information

ABSTRACT: Core–shell structured ZIF-8@ZIF-67 crystals are well-designed and prepared through a seed-mediated growth method. After thermal treatment of ZIF-8@ZIF-67 crystals, we obtain selectively functionalized nanoporous hybrid carbon materials consisting of nitrogen-doped carbon (NC) as the cores and highly graphitic carbon (GC) as the shells. This is the first example of the integration of NC and GC in one particle at the nanometer level. Electrochemical data strongly demonstrate that this nanoporous hybrid carbon material integrates the advantageous properties of the individual NC and GC, exhibiting a distinguished specific capacitance (270 F·g^{-1}) calculated from the galvanostatic charge–discharge curves at a current density of 2 A·g^{-1}. Our study not only bridges diverse carbon-based materials with infinite metal–organic frameworks but also opens a new avenue for artificially designed nanoarchitectures with target functionalities.

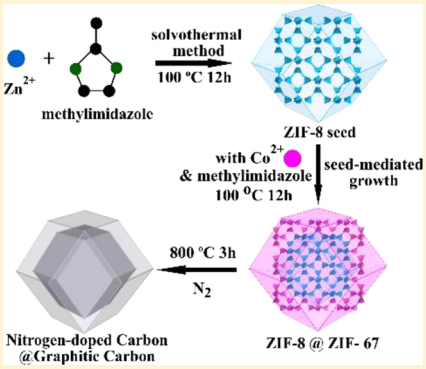

1. INTRODUCTION

Nanoporous carbons (NPCs), which have excellent chemical and mechanical stability, good electrical conductivity, a large specific surface area, and an adjustable pore structure, are attractive and significant materials for industrial applications as electrode materials, adsorbents, and catalyst supports.[1] To date, various carbon materials have been extensively studied for supercapacitor applications.[2] On the basis of previous research, high available surface areas are the predominant requirement for carbon-based electrodes used in supercapacitors.[3] Other factors such as accessible porous structures, good electrical conductivity, and surface functionalities also contribute to improve the capacitance.[4] Heteroatom doping (e.g., B, N, P) has been demonstrated as an effective strategy to enhance the capacitance of a carbon electrode through ameliorating the surface wettability and offering reversible pseudocapacitance effects.[5] Alternatively, the introduction of metals can provide additional functionalities in the carbon matrix and further promotes the applications of carbon materials, especially as electrode materials.[6] For example, the crystallinity and electrical conductivity of carbons can be remarkably improved by the incorporation of some specific metals (Fe, Co, and Ni) due to their effect of catalytic graphitization of amorphous carbon.[7] Therefore, heteroatom-doped and/or metal-modified carbons are very promising for future applications (e.g., supercapacitor) and attract much research interest.

Since the first report on metal–organic frameworks (MOFs)-derived NPCs by Xu et al.,[8] several types of NPCs have been prepared by carbonization of MOFs. The parent MOFs assembled from metal ions (or clusters) with bridging organic linkers have many fascinating properties, such as an ultrahigh surface area, tunable compositions, and diverse structural topologies. In some cases, MOFs are considered as sacrificial templates, and additional carbon sources such as furfuryl alcohol are introduced into the micropores of MOFs, followed by polymerization and carbonization, to prepare NPCs.[9] In contrast, direct carbonization of MOFs is found to be a straightforward route for the preparation of NPCs possessing an extremely high surface area, heteroatom doping, and functional metal species.[10] In all the previous works, however, NPCs are prepared from a single MOFs precursor, and therefore the expected functionalities are very limited.[11] In order to realize a high surface area, additional carbon sources (e.g., furfuryl alcohol) have been often filled in the MOFs, but the obtained NPCs are mainly composed of micropores, which

Received: November 10, 2014
Published: January 12, 2015

DOI: 10.1021/ja511539a
J. Am. Chem. Soc. 2015, 137, 1572–1580

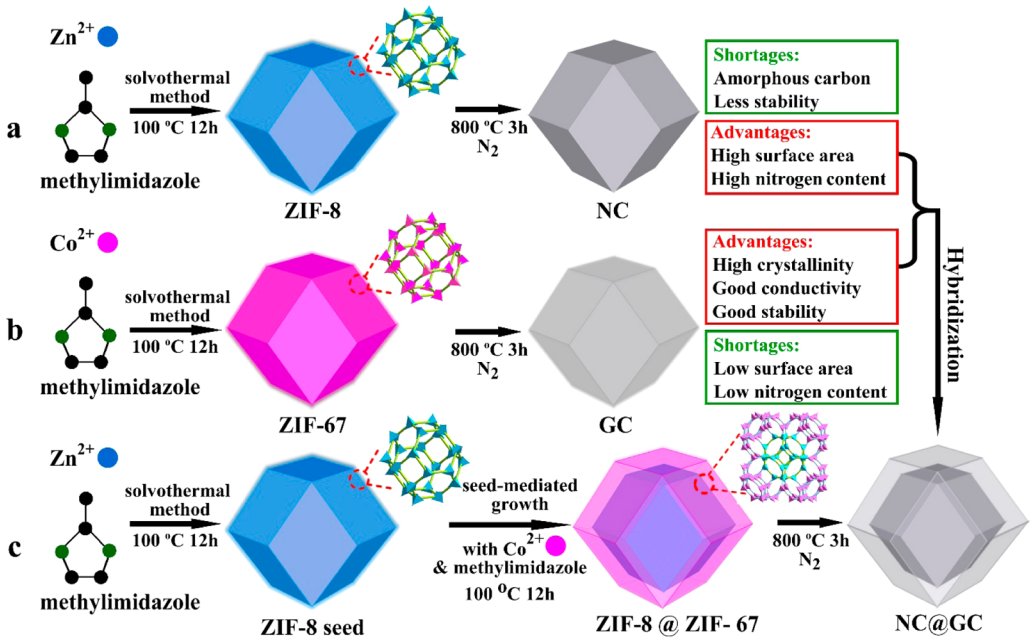

Figure 1. Synthetic scheme for the preparation of (a) ZIF-8 crystals and NC, (b) ZIF-67 crystals and GC, and (c) core–shell ZIF-8@ZIF-67 crystals and NC@GC.

suffer a diffusion limitation in supercapacitor application.[8,9a,11e] In addition, in the previous works, both high N content and highly graphitic structure are difficult to be realized at the same time because the N content largely decreases during the graphitization of NPCs.[10d,11d,12a] The high porosity of NPCs is also seriously sacrificed during the graphitization process.[12b] To overcome these issues, heterogeneous hybridization is an effective methodology to fuse the advantages of different materials and endows the hybrid materials with novel chemical and physical properties and interfacial functionality.[13] Our target in this study is to realize selectively functionalized NPCs derived from core–shell MOFs, which can bring out novel chemical and physical properties that are not attainable from a single MOFs precursor.

A zeolite imidazole framework (ZIF) is a well-known subfamily of MOFs formed through the coordination interaction between the metal ions and the imidazole derivatives.[14] Therefore, we set out to prepare core–shell MOFs (ZIF-8@ZIF-67) crystals, which consist of ZIF-8 ($[Zn(MeIm)_2]_n$) (MeIm = 2-methylimidazole) crystals as the core and ZIF-67 ($[Co(MeIm)_2]_n$) crystals as the shell, through a seed-mediated growth method that is usually adopted to prepare core–shell structured materials.[15] By thermal treatment of ZIF-8@ZIF-67 crystals, novel selectively functionalized nanoporous nitrogen-doped carbon@graphitic carbon (NC@GC) materials consisting of nitrogen-doped carbon (NC) as the core and highly graphitic carbon (GC) as the shell are successfully prepared (Figure 1). Nanoporous NC and GC materials have demonstrated different advantageous properties. Nanoporous NC prepared from ZIF-8 crystals has a relatively high N content of 16 wt % and a large surface area of 1499 $m^2 \cdot g^{-1}$, but the carbon is in an amorphous state. In contrast, nanoporous GC prepared from ZIF-67 crystals possesses highly graphitic walls with good conductivity due to the catalytic graphitization effect of well-dispersed Co species in the parent ZIF-67 crystals, but the surface area and N content are sacrificed. Our novel NC@GC materials prepared from core–shell structured MOFs (ZIF-8@ZIF-67) reasonably integrate the advantageous properties of both NC and GC, including the high surface area, high N content, and graphitic structure. Furthermore, the NC@GC materials possess interconnected hierarchically micro/mesoporous structure originated from the core–shell ZIF-8@ZIF-67, which are favorable in supercapacitor. As expected, our nanoporous NC@GC electrode displayed a superior electrochemical performance in terms of capacitance and retention in comparison with nanoporous NC and GC electrodes prepared from single ZIF-8 and ZIF-67 crystals, respectively. This study not only bridges diverse carbon-based materials with infinite MOFs but also opens a new avenue for artificially designed nanoarchitectures with target functionalities.

2. EXPERIMENTAL SECTION

2.1. Chemicals. Zinc nitrate hexahydrate ($Zn(NO_3)_2 \cdot 6H_2O$, 99%) and cobalt chloride ($CoCl_2$) were purchased from Sigma-Aldrich Chemical Co. 2-Methylimidazole (MeIm, purity 99%), hydrofluoric acid, and methanol were obtained from Nacalai Tesque Reagent Co. All the chemicals were used without further purification.

2.2. Preparation of ZIF-8 Seeds with Different Particle Sizes. In a typical synthesis of ZIF-8 with a diameter of ~4 μm, methanolic solutions of zinc nitrate hexahydrate (810 mg, 40 mL) and methanolic solutions of MeIm (526 mg, 40 mL) were mixed under stirring. Then the mixture was transferred into an autoclave and was kept at 100 °C for 12 h. The white powder was collected by centrifugation, washed several times with methanol, and dried at 80 °C. When the mixed methanolic solution of zinc nitrate hexahydrate and MeIm was kept at room temperature (22 °C) for 12 h, the white particles of ZIF-8 with a diameter of 500 nm were precipitated. The size of ZIF-8 could be further decreased to ~50 nm by adding polyvinylpyrrolidone (PVP) as the capping agent and kept the reaction at room temperature.

2.3. Preparation of ZIF-67. In the synthesis of ZIF-67 with a diameter of ~5 μm, a methanolic solutions (80 mL) of cobalt chloride (519 mg), polyvinylpyrrolidone (PVP) (600 mg) and MeIm (2630 mg) were mixed under stirring. Then the mixture was kept reaction at room temperature for 12 h. The bright purple powder of ZIF-67 was collected by centrifugation, washed several times with methanol, and dried at 80 °C.

DOI: 10.1021/ja511539a
J. Am. Chem. Soc. 2015, 137, 1572–1580

2.4. Preparation of Core–Shell ZIF-8@ZIF-67 Crystals. In a typical synthesis of core–shell ZIF-8@ZIF-67 crystals with micrometer-size, ZIF-8 seeds (80 mg) with diameter of ~4 μm were first well-dispersed in methanol (10 mL) under sonication for 30 min. After stirring for 20 min, a methanolic solution of cobalt chloride (177 mg, 3 mL) and a methanolic solution of MeIm (895 mg, 3 mL) were stepwise injected into the above mixture. After stirring for another 5 min, the mixture was transferred into an autoclave and kept at 100 °C for 12 h. During this time, the core–shell ZIF-8@ZIF-67 crystals were obtained. After cooling to room temperature, the resulting sample was collected by centrifugation, washed several times with methanol, and dried at 80 °C. The molar ratio of Co^{2+}/Zn^{2+} in the obtained ZIF-8@ZIF67 crystals under these typical conditions was 0.26. The shell thickness of ZIF-67 can be tuned by changing the amounts of methanolic solutions of cobalt chloride and MeIm. The obtained core–shell ZIF-8@ZIF-67 crystals with micrometer-size are noted as ZIF-8@ZIF-67(x), where x indicates the molar ratio of Co^{2+}/Zn^{2+} in the product.

2.5. Carbonization of Core–Shell ZIF-8@ZIF-67 Crystals. Core–shell ZIF-8@ZIF-67 crystals with micrometer-size were thermally converted to NC@GC materials through carbonization under a N_2 flow at 800 °C for 3 h, with a heating rate of 2 °C·min^{-1}. After that, the obtained samples were washed extensively by HF solution (10 wt %) to remove the deposited Zn and Co species. As a control experiment, two types of NPCs were prepared by single precursors (ZIF-8 and ZIF-67 with micrometer-size) under the same thermal conditions, which are noted as NC and GC, respectively.

2.6. Electrochemical Measurements. The electrochemical measurements were conducted in a standard three-electrode electrochemical cell. Platinum and Ag/AgCl (3 M KCl) electrodes were selected as the counter electrode and reference electrode, respectively. The working electrode was prepared according to the following process. 1 mg of NC@GC materials derived from core–shell ZIF-8@ZIF-67 crystals was mixed with poly(vinylidine difluoride) (0.1 mg) and then dissolved in *N*-methylpyrrolidinone solvent (0.5 mL). The obtained slurry was homogenized by ultrasonication, dropped onto graphite substrates (1 cm^2), and dried under infrared lamp to form the thin film on the electrodes. For comparison, nanoporous NC and GC materials were prepared from single ZIF-8 and ZIF-67 crystals, respectively. The electrochemical measurements were carried out using an electrochemical workstation (CHI 660E CH Instruments) in acid electrolyte (1.0 M H_2SO_4). The electrochemical properties of the supercapacitor were investigated by cyclic voltammetry (CV) and galvanostatic charge–discharge measurements. The charge–discharge current density varied from 2 to 20 A·g^{-1}. The specific capacitance was calculated from the galvanostatic charge–discharge curves using the following equation, $C = ((I \times \Delta t)/(m \times \Delta V))$, where I is charge–discharge current at a discharge time Δt (s), ΔV is the potential range, and m is the mass of active electrode materials.

2.7. Characterization. The morphology of the samples was characterized using a Hitachi SU-8000 field-emission scanning electron microscope (SEM) at an accelerating voltage of 5 kV. Transmission electron microscope (TEM) and elemental mapping analysis were measured by a JEM-2100 operated at 200 kV. Wide-angle powder X-ray diffraction (PXRD) patterns were measured by a Rigaku Rint 2000 X-ray diffractometer using monochromated Cu Kα radiation (40 kV, 40 mA) at a scanning rate of 2°·min^{-1}. N_2 adsorption–desorption isotherms were obtained using a Quantachrome Autosorb-iQ Automated Gas Sorption System at 77 K. The surface areas of ZIF-8, ZIF-67 and core–shell ZIF-8@ZIF-67 crystals were estimated based on the Brunauer–Emmett–Teller (BET) model and Langmuir model, respectively, by using the adsorption branch data in the relative pressure (P/P_0) range of 0.01–0.1. The surface areas of NC, GC and NC@GC were obtained based on the BET model by using the data of adsorption branches in the relative pressure (P/P_0) range of 0.05–0.5. The total pore volumes and pore-size distributions were calculated from the adsorption branches of isotherms based on the density functional theory (DFT) method. Thermogravimetric (TG) analysis was carried out using a Hitachi HT-Seiko Instrument Exter 6300 TG/DTA in N_2 heating from room temperature to 900 °C at 5 °C·min^{-1}. X-ray photoelectron spectroscopy (XPS) spectra were measured at room temperature using a PHI Quantera SXM (ULVAC-PHI) instrument with an Al Kα X-ray source. The region of survey spectra is 0 to 1400 eV and the region of high-resolution N 1s spectra is 392 to 412 eV. The percentage of N was calculated from the XPS survey spectrum by using N 1s peak. All the binding energies were calibrated via referencing to C 1 s binding energy (285.0 eV).

3. RESULTS AND DISCUSSION

3.1. Synthesis of Core–Shell ZIF-8@ZIF-67 Crystals. The core–shell MOFs (ZIF-8@ZIF-67) were prepared by a seed-mediated growth technique, as illustrated in Figure 1c. ZIF-8 and ZIF-67 are possible candidates for the preparation of core–shell MOFs (ZIF-8@ZIF-67) due to their isoreticular structures as $[M(MeIm)_2]_n$ (M = Zn for ZIF-8 and Co for ZIF-67) and their similar unit cell parameters between ZIF-8 ($a = b = c = 16.9910$ Å)[14a] and ZIF-67 ($a = b = c = 16.9589$ Å),[14b] which were determined by single crystal X-ray diffraction studies. To achieve this goal, uniformly sized ZIF-8 seeds were first synthesized by the coordination reaction of Zn^{2+} ions and MeIm. Scanning electron microscope (SEM) images confirmed that the obtained ZIF-8 consisted of uniformly dispersed crystals of rhombic dodecahedral shape, and the diameters of ZIF-8 were successfully tuned from 50 nm to 4 μm by tailoring the synthetic conditions (Figure S1a–c). As mentioned in the Experimental Section, in a typical synthesis, the methanolic solution containing zinc nitrate hexahydrate and MeIm was kept at room temperature, and the ZIF-8 crystals with a diameter of around 500 nm were precipitated. When PVP was added as the capping agent, the size of the ZIF-8 crystals was significantly decreased to around 50 nm. When the methanolic solution containing zinc nitrate hexahydrate and MeIm was transferred into an autoclave and the reaction was kept at 100 °C, the micrometer-sized ZIF-8 crystals were precipitated. The ZIF-67 crystals of rhombic dodecahedral shape with a diameter of 5 μm were obtained by mixing a methanolic solutions of cobalt chloride, PVP and MeIm and keeping the reaction at room temperature (Figure S1d).

For the preparation of core–shell ZIF-8@ZIF-67 crystals, here we selected ZIF-8 seeds with a diameter of 500 nm or 4 μm due to their better dispersity than ZIF-8 with a diameter of 50 nm. The good dispersity is quite important for uniform coating with the ZIF-67 shell. After adding a methanolic solution of $CoCl_2$, the Co^{2+} ions were immobilized on the surface of ZIF-8 seeds through the coordinative interaction with MeIm units exposed on the surface, followed by the growth of the ZIF-67 shell via the interaction with additive MeIm linkers. It is noted that ZIF-8 crystals are white, while ZIF-67 crystals are bright purple. After increasing the feeding ratio of Co^{2+}/Zn^{2+} during synthesis, the color of core–shell ZIF-8@ZIF-67 crystals gradually changed from white to pink, lavender, and bright purple (Figure S2), indicating the increased shell thicknesses of the ZIF-67 layer. The obtained core–shell MOFs crystals by using ZIF-8 seeds with a diameter of 4 μm were abbreviated as ZIF-8@ZIF-67(x), where x represented the corresponding molar ratios of Co^{2+}/Zn^{2+} in the products that were precisely determined by inductively coupled plasma (ICP) analysis.

In another experiment, we attempted to prepare core–shell ZIF-67@ZIF-8 crystals using the same protocol. However, no core–shell structures were observed. As seen in Figure S3a, a mixture of ZIF-8 crystals (300 nm) and ZIF-67 crystals (5 μm) was obtained. After shaking and standing the mixture for some

DOI: 10.1021/ja511539a
J. Am. Chem. Soc. 2015, 137, 1572–1580

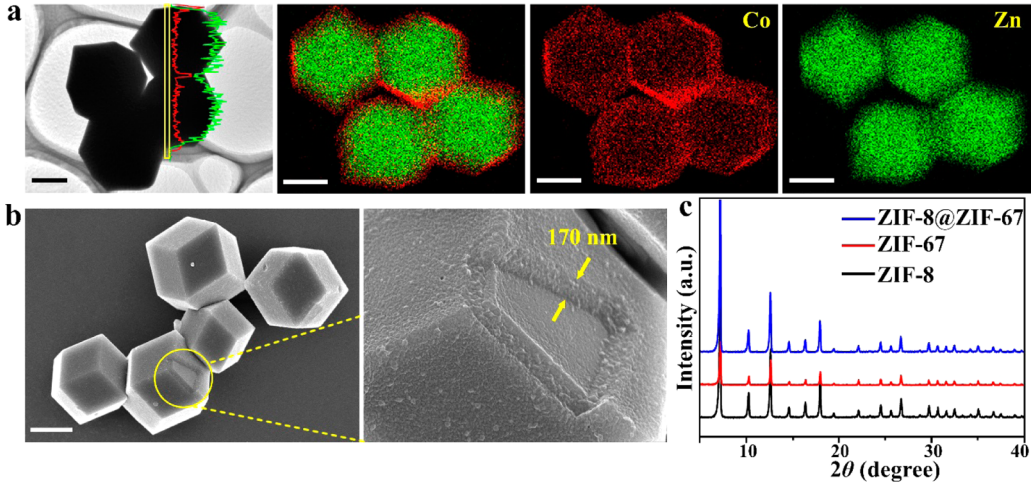

Figure 2. (a) TEM image and elemental mappings of the core−shell ZIF-8@ZIF-67(0.26) crystals, (b) SEM images of core−shell ZIF-8@ZIF-67(0.26) crystals, and (c) wide-angle PXRD patterns of as-synthesized ZIF-8, ZIF-67, and ZIF-8@ZIF-67(0.26) crystals. The scale bars are all 2 μm.

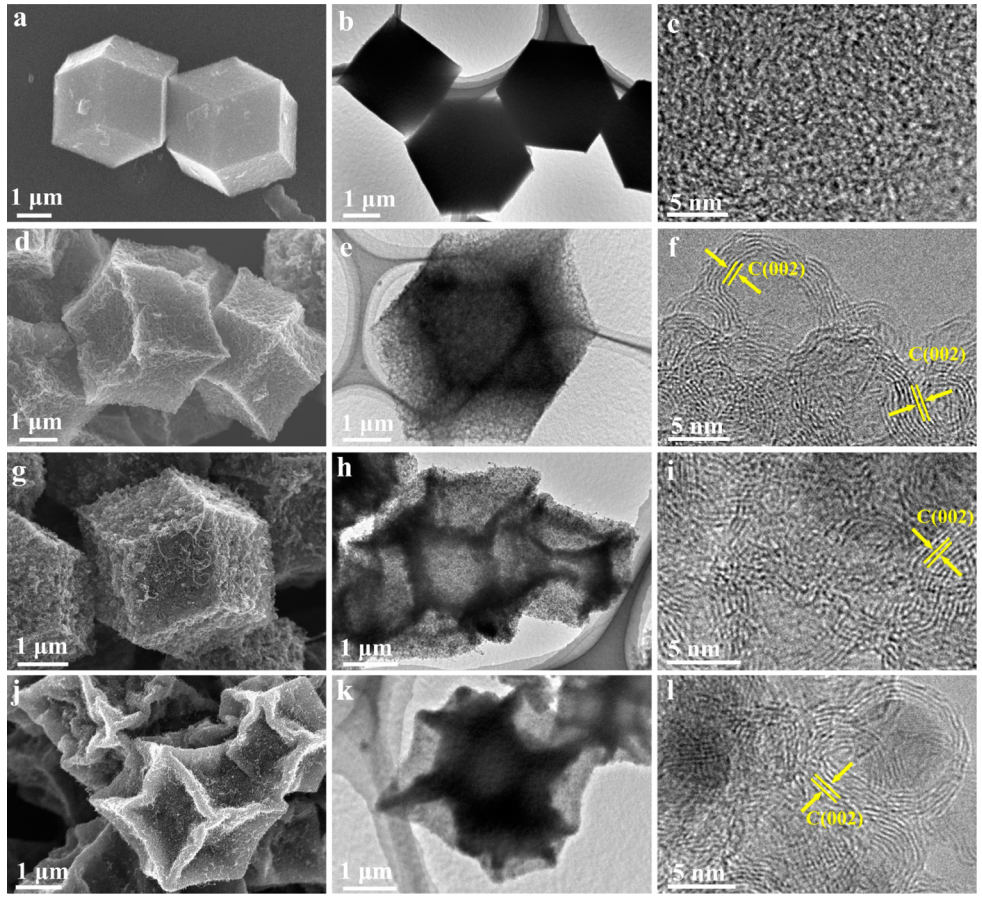

Figure 3. SEM images (a,d,g,j), TEM images (b,e,h,k), and HRTEM images (c,f,i,l) of NC (a−c), GC (d−f), NC@GC(0.05) (g−i), and NC@GC(0.35) (j−l).

time (Figure S3b,c), the micrometer-sized ZIF-67 crystals first precipitated and separated with ZIF-8 crystals, suggesting the failure of preparation of core−shell ZIF-67@ZIF-8. This was most likely due to the fast nucleation reaction of ZIF-8 crystals, which did not favor heterogeneous seed-induced nucleation on the surface of ZIF-67 seeds. Thus, it is difficult to coat the ZIF-67 seeds with the ZIF-8 layer under the similar synthetic condition.

The obtained core−shell ZIF-8@ZIF-67 crystals were carefully characterized. Figure 2a shows the TEM image, line scan, and elemental mappings for the representative ZIF-8@ZIF-67(0.26) crystals consisting of ZIF-8 cores and ZIF-67 shells. The molar ratio of Co^{2+}/Zn^{2+} detected by energy-dispersive X-ray (EDX) analysis was 0.26, which coincided with ICP data. As further proven by elemental mapping analysis (Figure S4), the core size and the shell thickness of ZIF-8@ZIF-67 crystals were easily controlled by using different sizes of

DOI: 10.1021/ja511539a
J. Am. Chem. Soc. 2015, 137, 1572−1580

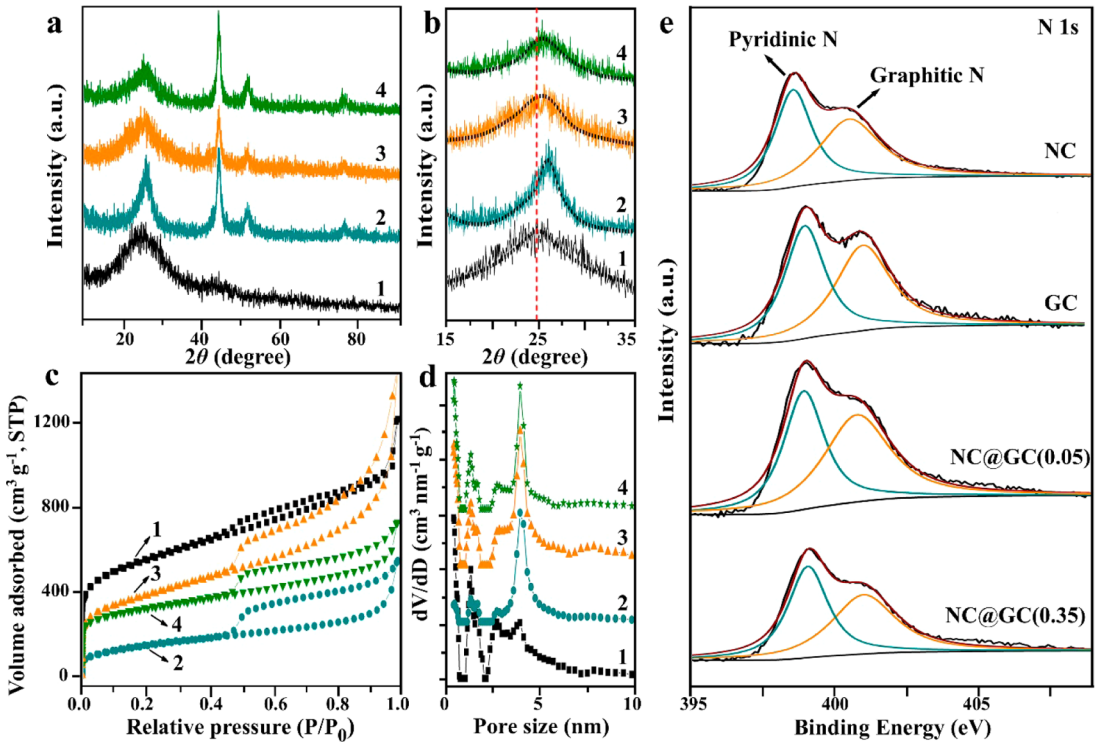

Figure 4. (a) Wide-angle XRD patterns, (b) enlarged XRD diffraction peaks, (c) N_2 adsorption−desorption isotherms, (d) pore-size distributions, and (e) high-resolution N 1s spectrum of the (1) NC, (2) GC, (3) NC@GC(0.05), and (4) NC@GC(0.35) samples. For clarity, the isotherms for (1) and (4) are offset by 100 and 50 $cm^3 \cdot g^{-1}$, respectively. The pore-size distribution curves for (2), (3), and (4) are offset vertically by 0.05, 0.10, and 0.15 $cm^3 \cdot nm^{-1} \cdot g^{-1}$, respectively.

ZIF-8 seeds and changing the feeding ratios of Co^{2+}/Zn^{2+} during the synthesis, respectively. As shown in Figure 2b, core−shell ZIF-8@ZIF-67(0.26) crystals show well-defined rhombic dodecahedral morphology, which corresponds to the original morphology of ZIF-8 seeds (Figure S1). As shown in Figure 2b, when the edge part with cracks was observed, it was found that the ZIF-67 shell uniformly coated ZIF-8 core with a thickness of 170 nm. The wide-angle PXRD patterns of ZIF-8, ZIF-67 and core−shell ZIF-8@ZIF-67(0.26) crystals provided a better understanding of the core−shell crystals (Figure 2c). The positions of diffraction peaks of our prepared ZIF-8 and ZIF-67 crystals corresponded to the PXRD patterns simulated from single crystal structures of ZIF-8[14a] and ZIF-67.[14b] The unit cell parameters estimated from our experimental PXRD pattern were $a = b = c = 17.0605$ Å for the prepared ZIF-8 crystals and were $a = b = c = 16.9687$ Å for the prepared ZIF-67 crystals. Because of the similar unit cell parameters of ZIF-8 and ZIF-67 crystals, we can anticipate that the core−shell ZIF-8@ZIF-67 crystals are successfully prepared most likely via epitaxial growth and exhibit topological information identical to those of the ZIF-8 and ZIF-67 crystals. The unit cell parameters of ZIF-8@ZIF-67(0.26) crystals ($a = b = c = 17.0140$ Å) are intermediate to those of ZIF-8 ($a = b = c = 17.0605$ Å) and ZIF-67 ($a = b = c = 16.9687$ Å), which were all calculated from the experimental PXRD patterns.

The porosity of ZIF-8, ZIF-67, and core−shell ZIF-8@ZIF-67(0.26) crystals was measured by N_2 adsorption−desorption isotherms. As shown in Figure S5a, all of the samples displayed type I isotherms with steep N_2 uptakes at low relative pressure, which is typically associated with microporosity. The Brunauer−Emmett−Teller (BET) surface areas (S_{BET}), Langmuir surface areas ($S_{Langmuir}$), total pore volumes (V_{pore}), and pore sizes are summarized in Table S2. It is observable that the pore sizes for all three samples are the same. The surface area and the pore volume of ZIF-8@ZIF-67(0.26) crystals increased almost 10% in comparison to those of ZIF-8 and ZIF-67 crystals. Thus, there is no serious pore blocking at the interface between core ZIF-8 and shell ZIF-67 crystals. As clearly seen in wide-angle PXRD results (Figure 2c), the crystal structure and its lattice constant of ZIF-8 (core) are almost the same as those of ZIF-67 (shell). Therefore, the ZIF-67 shell can grow well on the surface of ZIF-8 crystals. As far as we know, the seed-mediated growth method reported here, for the first time, realized the preparation of novel core−shell ZIF-8@ZIF-67 crystals with controllable core sizes and adjustable shell thicknesses at the nanometer scale.

3.2. Thermal Conversion of Core−Shell ZIF-8@ZIF-67 Crystals to Nanoporous NC@GC Materials. The obtained ZIF-8@ZIF-67 crystals were thermally treated at 800 °C under a N_2 flow. Thermogravimetric (TG) curves for ZIF-8, ZIF-67, and ZIF-8@ZIF-67(0.26) crystals measured under a N_2 atmosphere are shown in Figure S6. Core−shell ZIF-8@ZIF-67(0.26) crystals were thermally stable up to 470 °C. This stability was almost the same as ZIF-67 crystals (460 °C) but was lower than ZIF-8 crystals (550 °C). Then the weight of the crystals decreased rapidly along with the continued increase of temperature. During the heat treatment under N_2 atmospheres, organic linkers thermally carbonized into carbon networks, and parts of organic linkers decomposed and evaporated in the form of small molecules (e.g., H_2O, CO_2).[11c,16] Compared to the initial weight of ZIF-8, ZIF-67, and ZIF-8@ZIF-67(0.26) crystals, a 49−56 wt % loss (Table S3) was detected at 900 °C by TG analysis. After the carbonization, the products were washed with an HF solution to remove the residual Zn and/or

DOI: 10.1021/ja511539a
J. Am. Chem. Soc. 2015, 137, 1572−1580

Table 1. Surface Areas and Total Pore Volumes of NC, GC, NC@GC(0.05), and NC@GC(0.35)

sample	S_{BET} ($m^2 \cdot g^{-1}$)	S_{micro} ($m^2 \cdot g^{-1}$)	S_{micro}/S_{BET} (%)	V_{pore} ($cm^3 \cdot g^{-1}$)	V_{micro} ($cm^3 \cdot g^{-1}$)	V_{micro}/V_{pore} (%)	N content (atomic %)
NC	1499	378	25.2	1.31	0.184	14	16.1
GC	496	49	10.0	0.71	0.015	2.1	5.7
NC@GC(0.05)	1276	274	21.5	1.78	0.134	7.5	10.6
NC@GC(0.35)	813	120	14.7	0.89	0.036	4.0	8.5

Co species. NC, GC, and NC@GC(x) samples were prepared from ZIF-8, ZIF-67, and ZIF-8@ZIF-67(x), respectively.

As revealed by SEM images (Figure 3a), the obtained nanoporous NC particles retained the original rhombic dodecahedron shape from the parent ZIF-8 and exhibited a smooth surface without any large pores or cracks. In contrast, the nanoporous GC particles prepared from ZIF-67 shrank significantly and showed a distorted, bumpy surface (Figure 3d). A similar situation was observed with NC@GC particles prepared from ZIF-8@ZIF-67 crystals (Figure 3g,j). With the increase of ZIF-67 shell thickness, the NC@GC(0.35) particles that carbonized from ZIF-8@ZIF-67(0.35) with a thick ZIF-67 shell displayed a more seriously distorted surface than NC@GC(0.05) carbonized from ZIF-8@ZIF-67(0.05) with a thin ZIF-67 shell (Figure 3g,j). A more detailed porous structure and graphitic degree of the samples were investigated by TEM and high-resolution TEM (HRTEM). As seen in Figure 3c, no graphitic carbon structures were observed in NC particles, indicating that the particles were composed of disordered carbon (amorphous carbon) networks. Furthermore, there were no distinct pores shown in NC (Figure S7a) due to the mainly micropores with size smaller than 2 nm. In contrast, both GC and NC@GC particles showed distinct mesopores over the particle surface and abundant layered graphitic carbon structures with a typical distance value of graphite (0.334 nm), as revealed in Figure 3f,i,l and Figure S7b−d. Through careful observation by HRTEM, it was found that the graphitic carbons were formed by catalytic graphitization of amorphous carbon on the deposited Co nanoparticles.[17] Most of the Co nanoparticles were in uniform size and spherical shape (with diameter of around 3−4 nm) and they were easily removed by chemical etching (Figure 3f and Figure S7b−d), but there were some remaining Co nanoparticles with large size (over 7 nm) enclosed by well-developed graphitic layers. Because of such protection, it was difficult to completely remove the Co nanoparticles. The graphitization of amorphous carbon and the removal of Co species are supposed to induce the creation of a bumpy (rough) surface, as mentioned above (Figure 3). The particle shapes observed from TEM images (Figure 3b,e,h,k) were in accordance with SEM images (Figure 3a,d,g,j). From the elemental mapping analysis, it was revealed that the N element was more concentrated at the center of the particles, while the remaining Co nanoparticles were mostly observed only in the shell region (Figure S8). Thus, NC@GC particles with nitrogen-doped amorphous carbon cores and highly graphitic carbon shells were successfully obtained.

Wide-angle XRD patterns for nanoporous NC exhibited two broad diffraction peaks at 25° and 44° that are identical to the (002) and (101) diffractions of amorphous carbon (Figure 4a). In the case of GC, NC@GC(0.05), and NC@GC(0.35), the (002) diffraction peaks were significantly shifted toward 26°, suggesting the formation of a graphitic carbon structure (Figure 4b).[18] The other intense diffraction peaks located at around 44° and 51° were indexed to the (111) and (200) diffractions of face-centered-cubic (*fcc*) Co crystal (Figure 4a).[17] The average particle sizes of the remaining Co nanoparticles not completely dissolved by HF treatment were estimated to be around 7−8 nm, which coincides with the TEM data (Figure 3l).

The surface areas and pore-size distributions were investigated by N_2 adsorption−desorption isotherms (Figure 4c,d). The sharp uptakes at low relative pressure (<0.05) indicated the presence of micropores. The hysteresis loops and the gradual uptakes at a relative pressure range from 0.45 to 1.0, which were caused by the capillary condensation of N_2 in the mesopores with wide size distributions, were more distinct in the GC and NC@GC samples. Such hysteresis loops have often been observed in large mesoporous materials (e.g., SBA-type mesoporous silica).[19] Thus, the interconnected hierarchically micro/mesoporous structures were well-developed, as confirmed by the pore size distributions for each sample. The mesopores in GC and NC@GC were mainly generated by the carbonization process and the subsequent removal of Co nanoparticles with relatively small size (3−4 nm). Therefore, the mesopores are not uniform. The surface area (S_{BET}) and pore volume (V_{pore}) for the samples are summarized in Table 1. The NC sample possessed a high surface area of 1499 $m^2 \cdot g^{-1}$, which was a bit lower than that of the parent ZIF-8 crystals (1727 $m^2 \cdot g^{-1}$). However, the surface area of the GC sample with a highly graphitic structure was dramatically decreased to 496 $m^2 \cdot g^{-1}$. The value is extremely low in comparison to the original ZIF-67 crystals (1738 $m^2 \cdot g^{-1}$) due to the collapse of the well-defined microporous structure of ZIF-67 caused by the graphitization of amorphous carbon.[10d,11c] Furthermore, the ratio of the microporous surface area (S_{micro}/S_{BET}) in NC (25.2%) is much higher than that in GC (10.0%), confirming the presence of a large amount of mesopores in GC. As we expected, the surface areas of the NC@GC samples were the intermediate value between NC and GC. The NC@GC(0.05) sample with a thin GC shell showed a higher surface area (1276 $m^2 \cdot g^{-1}$) than the NC@GC(0.35) sample with a thick GC shell (813 $m^2 \cdot g^{-1}$), which also indirectly proves a successful tuning of the GC shell thickness.

The electronic state of N in the carbon matrix was carefully investigated by X-ray photoelectron spectroscopy (XPS). The N 1s spectra of all the samples can be mainly deconvoluted into two peaks centered at ∼398.8 and ∼400.8 eV, which are assignable to pyridinic-N and graphitic-N, respectively (Figure 4e). It was revealed that the N atoms in the pentagonal ring of the original imidazole units were mostly converted into two types of N states during the carbonization process. The N atoms were steadily doped into the carbon structure. The percentages of doped N content estimated from the XPS spectrum were 16.1 atomic% (for NC), 5.7 atomic% (for GC), 10.6 atomic% (for NC@GC(0.05)), and 8.5 atomic% (for NC@GC(0.35)). It is likely that the C−N bonds were partially destroyed during the catalytic graphitization process in the ZIF-67 crystals, thereby leading to the lower N content in the GC and NC@GC samples.[11d,12a,20]

3.3. Electrochemical Supercapacitors with NC@GC Electrodes. A supercapacitor is an electrochemical energy-

DOI: 10.1021/ja511539a
J. Am. Chem. Soc. 2015, 137, 1572−1580

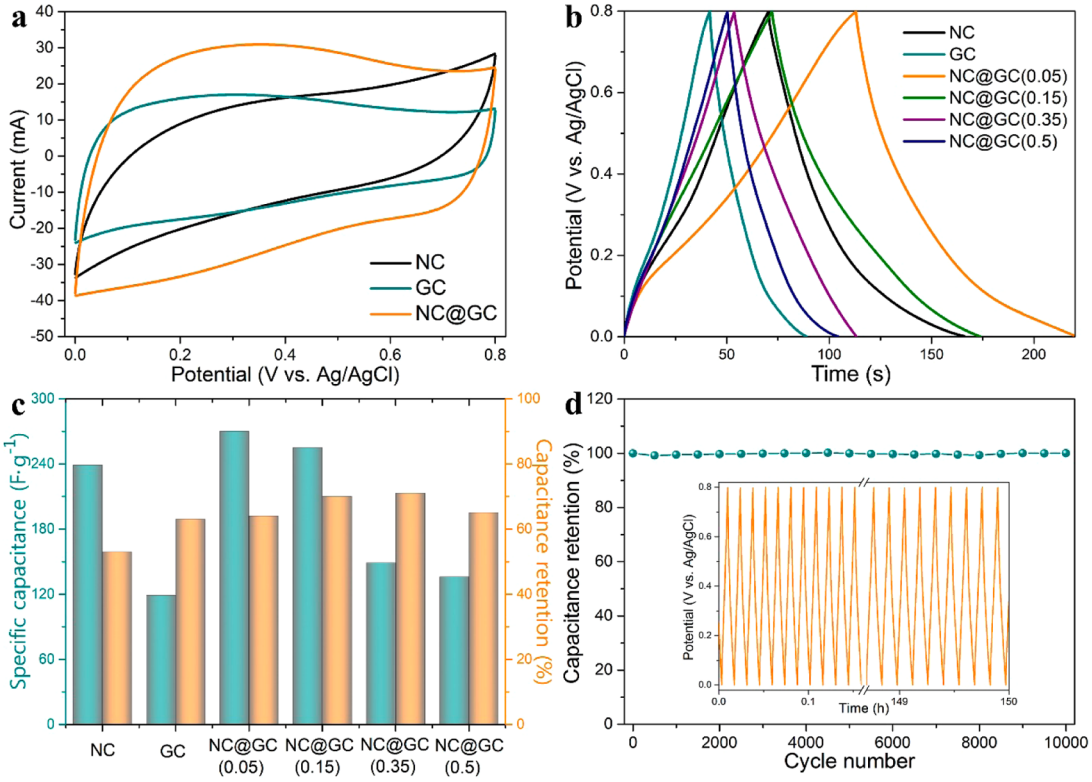

Figure 5. (a) Cyclic voltammograms at a potential scan rate of 200 mV·s^{-1} for NC, GC, and NC@GC(0.15). (b) Charge−discharge curves of NC, GC, NC@GC(0.05), NC@GC(0.15), NC@GC(0.35), and NC@GC(0.5) electrodes at a current density of 2 A·g^{-1}. (c) The specific capacitance values obtained at a current density of 2 A·g^{-1} and the respective capacitance retention ratios at a higher current density of 10 A·g^{-1} for NC, GC, NC@GC(0.05), NC@GC(0.15), NC@GC(0.35), and NC@GC(0.5) electrodes. (d) Cyclic stability of NC@GC(0.15) at a charge−discharge current density of 5 A·g^{-1} for 10,000 cycles. Inset shows the galvanostatic charge−discharge curves. All measurements were conducted in 1.0 M H_2SO_4 by using a three-electrode system.

storage device that can rapidly store and give out energy over a number of repeated cycles.[21] This unique feature makes it a promising candidate to meet the increasing power demands in the field of portable electronic devices, hybrid electric vehicles, and memory backup. To evaluate the electrochemical properties of NC, GC, and NC@GC electrodes, the cyclic voltammetry (CV) measurements using a standard three-electrode system were carried out in a 1 M H_2SO_4 aqueous electrolyte. The CV curves of NC, GC, and NC@GC electrodes conducted at different potential scan rates are shown in Figure S9. The distinct appearance of humps in the rectangular-like shape CV curves revealed that the capacitive response derived from the combination of electric double-layer capacitance (EDLC) and pseudocapacitance due to the nitrogen-doped in carbons.[5e,22,23c] The CV curves of NC, GC, and the representative NC@GC(0.15) electrodes at a high potential scan rate of 200 mV·s^{-1} are shown in Figure 5a. It is observed that NC displayed a distorted rectangular CV shape, whereas GC and NC@GC(0.15) electrodes present a quasi-rectangular CV shape. We infer that the ion-diffusion limitation in micropores is the predominant factor that leads to distorted rectangular CV shape at high potential scan rate.[2e,4b,23d] As concluded in Table 1, although NC possesses a higher surface area than GC and NC@GC, the ratios of micropores/mesopores are much higher in NC. Therefore, the serious ion-transfer resistance in the inner micropores, especially at a high potential scan rate, leads to the distorted CV shape.[2e,8,23d] In addition, nanoporous NC prepared from ZIF-8 crystals is in an amorphous state; therefore, the electrical conductivity mainly controlled by the crystallinity of carbon is not as satisfied as GC and NC@GC under high-rate operation.[22]

In order to evaluate the specific capacitance and get further insight into the electrochemical performance of the NC, GC, and NC@GC electrodes, a galvanostatic charge−discharge measurement that is a frequently used technique for capacitance evaluation was carried out at various current densities in a three-electrode system (Figure S10). The galvanostatic charge−discharge curves of all electrodes conducted at a current density of 2 A·g^{-1} are shown in Figure 5b. All of the electrodes displayed a quasi-linear appearance with a slight bend, implying the impact of pseudocapacitance derived from N doping.[2e,5e,22,23c,d] The specific capacitance values were calculated from the galvanostatic charge−discharge curves since it is considered to be a more accurate technique especially for EDLC materials.[9a,23c,d] As shown in Figure 5c, the specific capacitance values obtained at a current density of 2 A·g^{-1} are NC (239 F·g^{-1}), GC (119 F·g^{-1}), NC@GC(0.05) (270 F·g^{-1}), NC@GC(0.15) (255 F·g^{-1}), NC@GC(0.35) (149 F·g^{-1}), and NC@GC(0.5) (136 F·g^{-1}). The retention in specific capacitance at a higher current density of 10 A·g^{-1} for NC, GC, NC@GC(0.05), NC@GC(0.15), NC@GC(0.35), and NC@GC(0.5) is 53, 63, 64, 70, 71, and 65%, respectively. It is well-known that the high specific surface area of carbon materials usually leads to high capacitance, and N doping is able to increase the capacitance by bringing about pseudocapacitance and ameliorating surface wettability.[5a,23] Electrical conductivity, which is determined by the graphitic degree in carbon materials, is also crucial for capacitance by reducing the internal

DOI: 10.1021/ja511539a
J. Am. Chem. Soc. 2015, 137, 1572−1580

resistance. As discussed above, the NC@GC materials integrate the advantages of a high surface area and high N content in the NC core and a high graphitic degree in the GC shell, which can synergistically contribute to the high capacitance of an NC@GC electrode. Furthermore, the developed network of mesopores are also able to be accessed more freely and quickly by electrolyte ions,[24] even though the micropores are responsible for charge accommodation.[5a,b,12b,24b,25] Thus, the NC@GC(0.15) electrode consisting of the mediate graphitic carbon shell and highly porous carbon core exhibits the best electrochemical performance (specific capacitance of 255 $F{\cdot}g^{-1}$ with retention of 70%) compared to the other samples (Figure 5c) due to its optimized physicochemical properties. For a thinner GC shell, the capacitance value of the NC@GC(0.05) electrode is a bit higher (270 $F{\cdot}g^{-1}$); however, the retention in capacitance of NC@GC(0.05) electrode (64%) is much lower than that of the NC@GC(0.15) electrode (70%). Moreover, as we continue increasing the thickness of the GC shell, the specific capacitance value was found to be decreased in NC@GC(0.35) and NC@GC(0.5) electrodes. As demonstrated by the N_2 adsorption−desorption analysis (Table 1), the effective specific surface areas of NC@GC derived from ZIF-8@ZIF-67 crystals with a thicker ZIF-67 shell drastically declined due to the excessive graphitization of amorphous carbon in the thick GC shell, which ultimately decreased the capacitance value. The long-term cyclic stability of the representative NC@GC(0.15) electrode was investigated by using galvanostatic charge−discharge experiments at a current density of 5 $A{\cdot}g^{-1}$ within a potential window of 0−0.8 V (vs. Ag/AgCl). As shown in Figure 5d, the capacitance retention is almost 100% during all 10 000 cycles, indicating an excellent stability of NC@GC(0.15).

Further to demonstrate the importance of our hybrid structure (NC@GC), we simply mixed the NC and GC (mass ratio of NC is 0.9), and investigated their capacitive performance by CV and galvanostatic charge−discharge measurements (Figure S11). The specific capacitance value estimated from galvanostatic charge−discharge curve at a current density of 2 $A{\cdot}g^{-1}$ is only 69 $F{\cdot}g^{-1}$, which is much lower than NC@GC(270 $F{\cdot}g^{-1}$).

To the best of our knowledge, this capacitance value obtained from our study is significantly higher or comparable in comparison with the previously reported heteroatom-doped carbon materials, especially nitrogen-doped carbon materials (Table S4). Some reports show a little higher capacitances than our materials, but their current densities are too low (only 0.2 $A{\cdot}g^{-1}$).[5a,11b] To obtain high performance EDLC supercapacitor, we should consider a proper balance between surface area, pore volume, pore size distribution, graphitic degree and N content. Although the surface area of NC@GC is not exceptionally good enough compared with previous reports, we believe that the overall performance of our NC@GC material is due to the synergy of high specific surface area (1276 $m^2{\cdot}g^{-1}$), interconnected hierarchically micro/mesoporous structure, moderate N content (10.6 wt %), as well as optimized graphitic carbon shell thickness which allows easy and rapid diffusion of ions. As seen in the Table S4, other reported materials are not able to simultaneously possess so many kinds of excellent properties. Actually, practically improving one property will hamper other properties which results into decreased performance. In this study, the structure properties in our hybrid NC@GC material can be easily adjusted by tuning the shell thickness in the parent ZIF-8@ZIF-67 crystals, thus, superior electrochemical performance can be optimized successfully.

4. CONCLUSION

Core−shell ZIF-8@ZIF-67 crystals, which integrate the properties of single ZIF-8 and ZIF-67, are elaborately designed for the first time by applying a seed-mediated growth technique. The core sizes of ZIF-8 and the shell thicknesses of ZIF-67 can be tuned simply by using different sizes of ZIF-8 seeds and varying the feeding molar ratios of Co^{2+}/Zn^{2+}. After the direct carbonization of core−shell ZIF-8@ZIF-67 crystals, a new type of selectively functionalized NC@GC materials retain both the high surface area (up to 1276 $m^2{\cdot}g^{-1}$) and high N content (10.6 wt %) derived from core ZIF-8 and superior graphitic structure originated from shell ZIF-67. The optimized NC@GC exhibits a distinguished electrochemical performance as an electrode in supercapacitors. This study bridges infinite MOFs with diverse functional carbon-based materials and provides new insight into artificially designed nanomaterials.

■ ASSOCIATED CONTENT

Supporting Information

Additional SEM, TEM and STEM images, elemental mappings, N_2 adsorption−desorption isotherms, pore size distributions, TG curves, cyclic voltammograms, charge−discharge curves, etc. This material is available free of charge via the Internet at http://pubs.acs.org.

■ AUTHOR INFORMATION

Corresponding Author

yamauchi.yusuke@nims.go.jp

Notes

The authors declare no competing financial interest.

■ ACKNOWLEDGMENTS

This research was partially supported by the Grant-in-Aid for Young Scientists A (Research Project Number: 26708028) of the Japan Society for the Promotion of Science (JSPS), Japanese-Taiwanese Cooperative Program of the Japan Science and Technology Agency (JST), and The Canon Foundation.

■ REFERENCES

(1) (a) Liang, C. D.; Li, Z. J.; Dai, S. *Angew. Chem., Int. Ed.* **2008**, *47*, 3696. (b) Wu, Z. X.; Wu, W. D.; Liu, W. J.; Selomulya, C.; Chen, X. D.; Zhao, D. Y. *Angew. Chem., Int. Ed.* **2013**, *52*, 13764. (c) Fang, Y.; Zheng, G. F.; Yang, J. P.; Tang, H. S.; Zhang, Y. F.; Kong, B.; Lv, Y. Y.; Xu, C. J.; Asiri, A. M.; Zi, J.; Zhang, F.; Zhao, D. Y. *Angew. Chem., Int. Ed.* **2014**, *53*, 5366. (d) Fulvio, P. F.; Mayes, R. T.; Wang, X. Q.; Mahurin, S. M.; Bauer, J. C.; Presser, V.; McDonough, J.; Gogotsi, Y.; Dai, S. *Adv. Funct. Mater.* **2011**, *21*, 2208. (e) Chang, H.; Joo, S. H.; Pak, C. *J. Mater. Chem.* **2007**, *17*, 3078. (f) Tang, J.; Liu, J.; Torad, N. L.; Kimura, T.; Yamauchi, Y. *Nano Today* **2014**, *9*, 305.

(2) (a) Zhong, M. J.; Kim, E. K.; McGann, J. P.; Chun, S.-E.; Whitacre, J. F.; Jaroniec, M.; Matyjaszewski, K.; Kowalewski, T. *J. Am. Chem. Soc.* **2012**, *134*, 14846. (b) Jin, J.; Tanaka, S.; Egashira, Y.; Nishiyama, N. *Carbon* **2010**, *48*, 1985. (c) Lei, Z. B.; Bai, D.; Zhao, X. S. *Microporous Mesoporous Mater.* **2012**, *147*, 86. (d) Guo, H. L.; Gao, Q. M. *J. Power Sources* **2009**, *186*, 551. (e) Zhu, H.; Yin, J.; Wang, X.; Wang, H.; Yang, X. *Adv. Funct. Mater.* **2013**, *23*, 1305.

(3) (a) Pandolfo, A. G.; Hollenkamp, A. F. *J. Power Sources* **2006**, *157*, 11. (b) Aricò, A. S.; Bruce, P.; Scrosati, B.; Tarascon, J. M.; Schalkwijk, W. V. *Nat. Mater.* **2005**, *4*, 366.

(4) (a) Frackowiak, E.; Béguin, F. *Carbon* **2001**, *39*, 937. (b) Wang, D. W.; Li, F.; Liu, M.; Lu, G. Q.; Cheng, H. M. *Angew. Chem., Int. Ed.*

DOI: 10.1021/ja511539a
J. Am. Chem. Soc. 2015, 137, 1572−1580

2008, *47*, 373. (c) Datta, K. K. R.; Balasubramanian, V. V.; Ariga, K.; Mori, T.; Vinu, A. *Chem.—Eur. J.* **2011**, *17*, 3390.
(5) (a) Ania, C. O.; Khomenko, V.; Raymundo-Pinero, E.; Parra, J. B.; Beguin, F. *Adv. Funct. Mater.* **2007**, *17*, 1828. (b) Hulicova-Jurcakova, D.; Puziy, A. M.; Poddubnaya, O. I.; Suárez-García, F.; Tascón, J. M. D.; Lu, G. Q. *J. Am. Chem. Soc.* **2009**, *131*, 5026. (c) Salunkhe, R. R.; Kamachi, Y.; Torad, N. L.; Hwang, S. M.; Sun, Z. Q.; Dou, S. X.; Kim, J. H.; Yamauchi, Y. *J. Mater. Chem. A* **2014**, *2*, 19848. (d) Wang, D. W.; Li, F.; Chen, Z. G.; Lu, G. Q.; Cheng, H. M. *Chem. Mater.* **2008**, *20*, 7195. (e) Iyyamperumal, E.; Wang, S. Y.; Dai, L. M. *ACS Nano* **2012**, *6*, 5259. (f) Wu, Z. S.; Winter, A.; Chen, L.; Sun, Y.; Turchanin, A.; Feng, X. L.; Müllen, K. *Adv. Mater.* **2012**, *24*, 5130.
(6) (a) Hu, C. C.; Chang, K. H.; Lin, M. C.; Wu, Y. T. *Nano Lett.* **2006**, *6*, 2690. (b) Chen, Z.; Qin, Y. C.; Weng, D.; Xiao, Q. F.; Peng, Y. T.; Wang, X. L.; Li, H. X.; Wei, F.; Lu, Y. F. *Adv. Funct. Mater.* **2009**, *19*, 3420. (c) Wang, T.; Tang, J.; Fan, X. L.; Zhou, J. H.; Xue, H. R.; Guo, H.; He, J. P. *Nanoscale* **2014**, *6*, 5359.
(7) (a) Sevilla, M.; Fuertes, A. B. *Carbon* **2006**, *44*, 468. (b) Tang, J.; Wang, T.; Sun, X.; Guo, Y. X.; Xue, H. R.; Guo, H.; Liu, M. Z.; Zhang, X. X.; He, J. P. *Microporous Mesoporous Mater.* **2013**, *177*, 105. (c) Schaefer, Z. L.; Gross, M. L.; Hickner, M. A.; Schaak, R. E. *Angew. Chem., Int. Ed.* **2010**, *49*, 7045. (d) Yuan, J. Y.; Giordano, C.; Antonietti, M. *Chem. Mater.* **2010**, *22*, 5003.
(8) Liu, B.; Shioyama, H.; Akita, T.; Xu, Q. *J. Am. Chem. Soc.* **2008**, *130*, 5390.
(9) (a) Jiang, H.-L.; Liu, B.; Lan, Y.-Q.; Kuratani, K.; Akita, T.; Shioyama, H.; Zong, F. Q.; Xu, Q. *J. Am. Chem. Soc.* **2011**, *133*, 11854. (b) Almasoudi, A.; Mokaya, R. *J. Mater. Chem.* **2012**, *22*, 146.
(10) (a) Hu, M.; Reboul, J.; Furukawa, S.; Torad, N. L.; Ji, Q. M.; Srinivasu, P.; Ariga, K.; Kitagawa, S.; Yamauchi, Y. *J. Am. Chem. Soc.* **2012**, *134*, 2864. (b) Aiyappa, H. B.; Pachfule, P.; Banerjee, R.; Kurungot, S. *Cryst. Growth Des.* **2013**, *13*, 4195. (c) Chaikittisilp, W.; Hu, M.; Wang, H.; Huang, H. S.; Fujita, T.; Wu, K. C. W.; Chen, L. C.; Yamauchi, Y.; Ariga, K. *Chem. Commun.* **2012**, *48*, 7259. (d) Torad, N. L.; Salunkhe, R. R.; Li, Y. Q.; Hamoudi, H.; Imura, M.; Sakka, Y.; Hu, C.-C.; Yamauchi, Y. *Chem.—Eur. J.* **2014**, *20*, 7895. (e) Torad, N. L.; Hu, M.; Kamachi, Y.; Takai, K.; Imura, M.; Naito, M.; Yamauchi, Y. *Chem. Commun.* **2013**, *49*, 2521.
(11) (a) Lim, S.; Suh, L.; Kim, Y.; Yoon, M. Y.; Park, H.; Dybtsev, D. N.; Kim, K. *Chem. Commun.* **2012**, *48*, 7447. (b) Hu, J.; Wang, H. L.; Gao, Q. M.; Guo, H. L. *Carbon* **2010**, *48*, 3599. (c) Torad, N. L.; Hu, M.; Ishihara, S.; Sukegawa, H.; Belik, A. A.; Imura, M.; Ariga, K.; Yamauchi, Y.; Sakka, Y. *Small* **2014**, *10*, 2096. (d) Ma, S. Q.; Goenaga, G. A.; Call, A. V.; Liu, D. J. *Chem.—Eur. J.* **2011**, *17*, 2063. (e) Amali, A. J.; Sun, J.-K.; Xu, Q. *Chem. Commun.* **2014**, *50*, 1519.
(12) (a) Hulicova, D.; Kodama, M.; Hatori, H. *Chem. Mater.* **2005**, *17*, 1241. (b) Chmiola, J.; Yushin, G.; Dash, R.; Gogotsi, Y. *J. Power Sources* **2006**, *158*, 765.
(13) (a) Furukawa, S.; Hirai, K.; Nakagawa, K.; Takashima, Y.; Matsuda, R.; Tsuruoka, T.; Kondo, M.; Haruki, R.; Tanaka, D.; Sakamoto, H.; Shimomura, S.; Sakata, O.; Kitagawa, S. *Angew. Chem., Int. Ed.* **2009**, *48*, 1766. (b) Koh, K.; Wong-Foy, A. G.; Matzger, A. J. *Chem. Commun.* **2009**, 6162. (c) Song, X.; Kim, T.; Kim, H.; Kim, D.; Jeong, S.; Moon, H. R.; Lah, M. S. *Chem. Mater.* **2012**, *24*, 3065. (d) Li, T.; Sullivan, J. E.; Rosi, N. L. *J. Am. Chem. Soc.* **2013**, *135*, 9984.
(14) (a) Park, K. S.; Ni, Z.; Côté, A. P.; Choi, J. Y.; Huang, R. D.; Uribe-Romo, F. J.; Chae, H. K.; O'Keeffe, M.; Yaghi, O. M. *Proc. Natl. Acad. Sci. U. S. A.* **2006**, *103*, 10186. (b) Banerjee, R.; Phan, A.; Wang, B.; Knobler, C.; Furukawa, H.; O'Keeffe, M.; Yaghi, O. M. *Science* **2008**, *319*, 939.
(15) (a) Xie, B.; Song, J. W.; Ren, L. M.; Ji, Y. Y.; Li, J. X.; Xiao, F.-S. *Chem. Mater.* **2008**, *20*, 4533. (b) Xie, B.; Zhang, H. Y.; Yang, C. G.; Liu, S. Y.; Ren, L. M.; Zhang, L.; Meng, X. J.; Yilmaz, B.; Müller, U.; Xiao, F.-S. *Chem. Commun.* **2011**, *47*, 3945. (c) MacDonald, J. C.; Dorrestein, P. C.; Pilley, M. M.; Foote, M. M.; Lundburg, J. L.; Henning, R. W.; Schultz, A. J.; Manson, J. L. *J. Am. Chem. Soc.* **2000**, *122*, 11692. (d) Noveron, J. C.; Lah, M. S.; Sesto, R. E. D.; Arif, A. M.; Miller, J. S.; Stang, P. J. *J. Am. Chem. Soc.* **2000**, *124*, 6613.
(16) Yang, S. J.; Kim, T.; Im, J. H.; Kim, Y. S.; Lee, K.; Jung, H.; Park, C. R. *Chem. Mater.* **2012**, *24*, 464.
(17) (a) Tang, J.; Wang, T.; Pan, X. C.; Sun, X.; Fan, X. L.; Guo, Y. X.; Xue, H. R.; He, J. P. *J. Phys. Chem. C* **2013**, *117*, 16896. (b) Barakat, N. A. M.; Kim, B.; Park, S. J.; Jo, Y. H.; Jung, M.-H.; Kim, H. Y. *J. Mater. Chem.* **2009**, *19*, 7371.
(18) (a) Kim, J.; Ryoo, R.; Stevenson, K. J.; Johnston, K. P. *J. Phys. Chem. C* **2010**, *114*, 10796. (b) Yan, Z. X.; Cai, M.; Shen, P. K. *J. Mater. Chem.* **2012**, *22*, 2133.
(19) (a) Zhao, Y. Z.; Feng, J. L.; Huo, Q. S.; Melosh, N.; Fredrickson, G. H.; Chmelka, B. F.; Stucky, G. D. *Science* **1998**, *279*, 548. (b) Shen, S. D.; Garcia-Bennett, A. E.; Liu, Z.; Lu, Q. Y.; Shi, Y. F.; Yan, Y.; Yu, C. Z.; Liu, W. C.; Cai, Y.; Terasaki, O.; Zhao, D. Y. *J. Am. Chem. Soc.* **2005**, *127*, 6780.
(20) Ōya, A.; Ōtani, S. *Carbon* **1979**, *17*, 131.
(21) (a) Miller, J. R.; Simon, P. *Science* **2008**, *321*, 651. (b) Simon, P.; Gogotsi, Y. *Nat. Mater.* **2008**, *7*, 845.
(22) Ma, F. W.; Zhao, H.; Sun, L. P.; Li, Q.; Huo, L. H.; Xia, T.; Gao, S.; Pang, G. S.; Shi, Z.; Feng, S. H. *J. Mater. Chem.* **2012**, *22*, 13464.
(23) (a) Jeong, H. M.; Lee, J. W.; Shin, W. H.; Choi, Y. J.; Shin, H. J.; Kang, J. K.; Choi, J. W. *Nano Lett.* **2011**, *11*, 2472. (b) Hulicova, D.; Kodama, M.; Hatori, H. *Chem. Mater.* **2006**, *18*, 2318. (c) Zhao, L.; Fan, L. Z.; Zhou, M. Q.; Guan, H.; Qiao, S.; Antonietti, M.; Titirici, M.-M. *Adv. Mater.* **2010**, *22*, 5202. (d) Chen, L. F.; Zhang, X. D.; Liang, H. W.; Kong, M. G.; Guan, Q. F.; Chen, P.; Wu, Z. Y.; Yu, S. H. *ACS Nano* **2012**, *6*, 7092.
(24) (a) Liu, B.; Shioyama, H.; Jiang, H. L.; Zhang, X. B.; Xu, Q. *Carbon* **2010**, *48*, 456. (b) Frackowiak, E.; Lota, G.; Machnikowski, J.; Vix-Guterl, C.; Béguin, F. *Electrochim. Acta* **2006**, *51*, 2209.
(25) (a) Chmiola, J.; Yushin, G.; Gogotsi, Y.; Portet, C.; Simon, P.; Taberna, P. L. *Science* **2006**, *313*, 1760. (b) Raymundo-Pinñro, E.; Kierzek, K.; Machnikowski, J.; Béguin, F. *Carbon* **2006**, *44*, 2498.

DOI: 10.1021/ja511539a
J. Am. Chem. Soc. 2015, 137, 1572−1580